Electronic Supplementary Information

Zn^{2+}-intercalated $V_2O_5 \cdot nH_2O$ Derived from V_2CT_X MXene for Hyper-stable Zinc-Ion Storage

Xiaodong Zhu,[a,b] Wenjie Wang,[b] Ziyi Cao,[a,c] Shangpeng Gao,[b] Mason Oliver Lam Chee,[d] Xiang Zhang,[e] Pei Dong,[d] Pulickel M. Ajayan,[e] Mingxin Ye*[a] and Jianfeng Shen*[a]

[a]Institute of special materials and technology, Fudan University, Shanghai 200433, P. R. China

[b]Department of Materials Science, Fudan University, Shanghai 200433, P. R. China

[c]Department of Chemistry, Fudan University, Shanghai 200433, P. R. China

[d]Department of Mechanical Engineering, George Mason University, VA 22030, USA

[e]Department of Materials Science and Nano Engineering, Rice University, Houston 70054, USA

*Corresponding: mxye@fudan.edu.cn; jfshen@fudan.edu.cn

Experimental Section

Synthesis of Pre-Alkalized V_2CT_X

Vanadium (Aladdin reagent, 99.5 wt% purity), aluminum (Aladdin reagent, 99.5 wt% purity,), and graphite (Aladdin reagent, 99.95 wt% purity) powders were blended with the molar ratio of 2.0:1.16:1.0 and then ground for 10 h at 580 rotations per minute in isopropanol. Mixed powders were prepared by vacuum drying at 45 °C for 10 h. Subsequently, cold pressing mixed powders at 16 MPa and sintered in an argon atmosphere at 1510 °C for 4 h. Obtained MAX ceramics was grounded with a 200 mesh sieve.

Slowly add 1.0 g V_2AlC MAX to 50 mL of 40 wt% HF solution (SCR Co., GR grade). After continuous stirring at 35 °C for 72 hours, the resulting mixture solution was washed by centrifugation with deionized water several times until the pH value was ~7. Then, the black colloidal precipitate was freeze-dried for 48 hours to gain V_2CT_X MXene. Then, the V_2CTx powder was alkalization-treated by 6×10^{-3} M NaOH (Aladdin Reagent, 99.9 wt% purity) solution for 8 h. The product is then centrifuged and washed, and freeze-dried for 48 h.

Synthesis of V_2CT_X-$Zn_{0.25}V_2O_5\cdot nH_2O$ and Oxidized V_2CTx

0.25 g alkalized V_2CTx was added to 32 mL 0.2 M $ZnCl_2$ (SMBT Co., Ltd, GR grade) solution. After 1.0 h of strong stirring, slowly add 1.5 mL of H_2O_2 (Aladdin Reagent, Ltd, 30 wt%) solution into the dispersion, and then transfer to the autoclave. The one-pot hydrothermal reaction was carried out under 160 °C for 10 h. Then, V_2CT_X-$Zn_xV_2O_5\cdot nH_2O$ (VC−ZVO) was washed and then collected after freeze-dried for 72 h. The preparation of oxidized V_2CT_X is similar to the above method with 40 mL 0.015 wt% H_2O_2 solution under 160 °C for 10 h.

Synthesis of $V_2O_5\cdot1.6H_2O$ Nanobelts

0.32 g commercial V_2O_5 (Jinshan chemical test, 99 wt%) were added into 30 mL deionized water. After 20 min of strong stirring, 5 mL 30 wt% H_2O_2 solution was then slowly added into the solution. Then transfer the dispersion to the autoclave, and the facile hydrothermal reaction was carried out under 200 °C for 24 h. After cooling to room temperature, the reaction products were collected and obtained *via* freeze-dried for 72 h.

Physical Characterization

The crystal information of the samples was defined by X-ray diffraction (XRD, Bruker D8 ADVANCED X-ray powder diffractometer, Cu Kα radiation). The Fourier Transform Infrared Spectroscopy (FTIR, Nicolet Is10) was determined with a scan range from 2000 to 400 cm^{-1}. Field-emission scanning electron microscopy (SEM, Tescan MAIA3 XMH), transmission electron microscopy (TEM, JEOL JEM-2100 LaB6), and their EDX components were used to observe the microstructure information and elements distribution of the samples. The surface elements were evaluated by X-ray photoelectron spectroscopy (XPS, PHI 5000C&PHI5300). The specific surface area and pore size distribution of the samples were measured by the Brunauer-Emmett-Teller instrument (BET, Micromeritics ASAP 2020). The V K-edge X-ray absorption spectroscopy (XAS) data were collected on beamline BL14W1 at the Shanghai Synchrotron Radiation Facility (SSRF).

Electrochemical Measurements

CR2032 coin-type cells were used for electrochemical analysis. In detail, the working electrodes were made up of active material, carbon black (Aladdin reagent, 99.5%, ~30 nm) and polyvinylidene fluoride (PVDF) (Aladdin reagent) binder in a mass ratio of 7:2:1.0 was tightly mixed with 1-Methyl-2-pyrrolidinone (NMP) (Aladdin reagent, 99.5 wt%) to form a uniform slurry. It was coated on titanium substrate and dried in a vacuum oven at 60 °C for 14 h. The loading mass of the cathode is in the range of 1.6-1.8 mg. Zinc foil was used as the counter negative electrode, 3 M $Zn(CF_3SO_3)_2$ dissolved in deionized water as electrolyte, and glass microfiber filter membrane as the separator. The assembly process was carried out in an argon-filled glovebox (Mikrona). The rate performance, cycling capability, and GITT were carried out on the Land CT 2001A CELL test system in the range of 0.3-1.4 V at 25 °C. The capacity of the samples is calculated according to the mass of the active materials. In addition, the cyclic voltammetry curves of five scanning sections at each scanning rate were collected from the open circuit potential in a electrochemical workstation (PGSTAT302N, Metrohm) using a three-electrode set (0.3-1.4V vs Zn^{2+}/Zn). On the same electrochemical workstation, the EIS was measured in the frequency range of 10^5-0.01 Hz with 5 mV AC oscillation amplitude.

Computational Methods

All calculations based on density functional theory were operated by the Vienna Ab-initio Simulation Package (VASP) with projector-augmented wave (PAW) pseudopotentials. The exchange-correlation functional was described by the generalized gradient approximation (GGA) of Perdew-Burke-Ernzerhof (PBE). The kinetic energy cut-off was set to 520 eV, and k-points were generated by Monkhorst-Pack grid of 2 × 3 × 2. The energy tolerance and the allowed maximum Hellman-Feynman force on each atom were set to 10^{-6} eV and 0.01 eV $Å^{-1}$, respectively. The van der Waals dispersion correction was employed by the DFT-D2 method of Grimme. The LDA + U method was applied to the description of strongly correlated electrons for the density of states (DOS) calculations, with U of 3.1 eV for vanadium.[1]

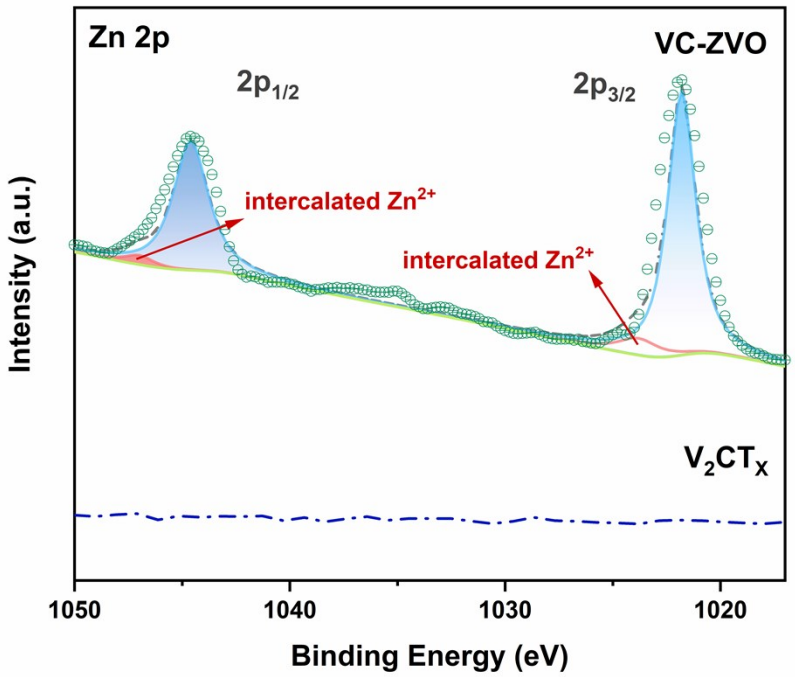

Fig. S1 XPS spectra of Zn 2p of V_2CT_X MXene and VC−ZVO.

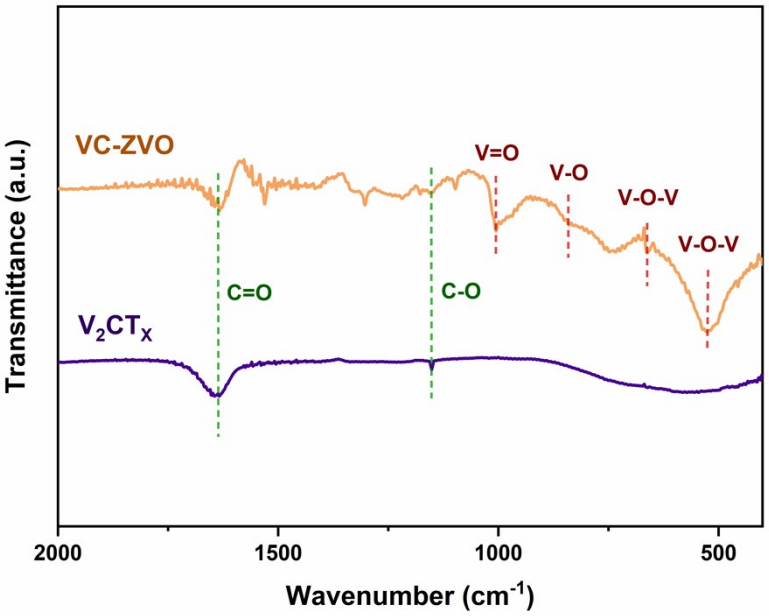

Fig. S2 FTIR spectra of V_2CT_X MXene and VC−ZVO.

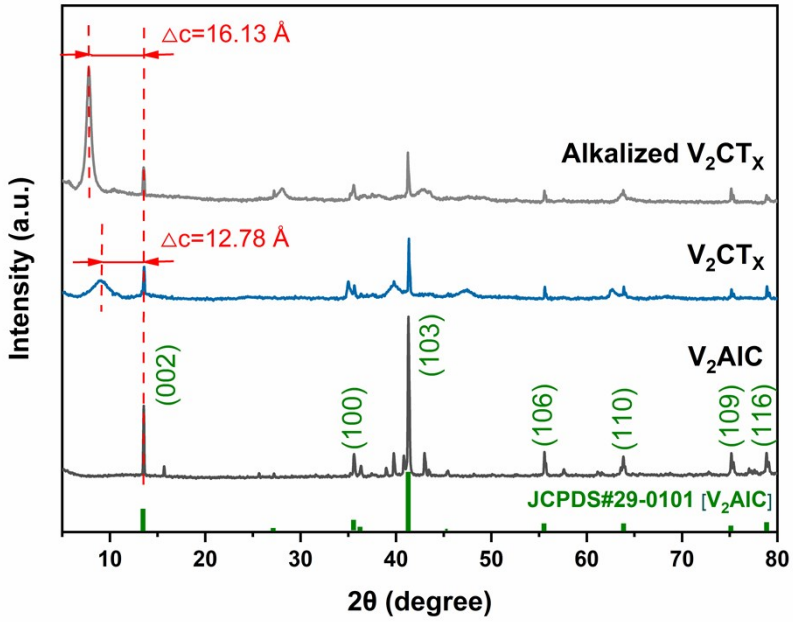

Fig. S3 XRD pattern of V_2AlC MAX, V_2CT_X MXene and alkalized V_2CT_X.

The XRD results in Figure S3 show that the main diffraction peaks of V_2AlC correspond to JCPDS# 29-0101,[2] which verifies the successful synthesis of V_2AlC MAX phase. After the etching process, most of the diffraction peaks of V_2AlC are weakened, and a new peak appeared on the (002) plane of V_2CTx at 9.01°. After alkalization, the (002) peak becomes sharper and shifts to a lower angle of 7.78°, indicating that Na^+ intercalation in the interlayer of V_2CTx leads to the expansion of interspace and a 1.136 nm gap between the layers of V_2CTx.

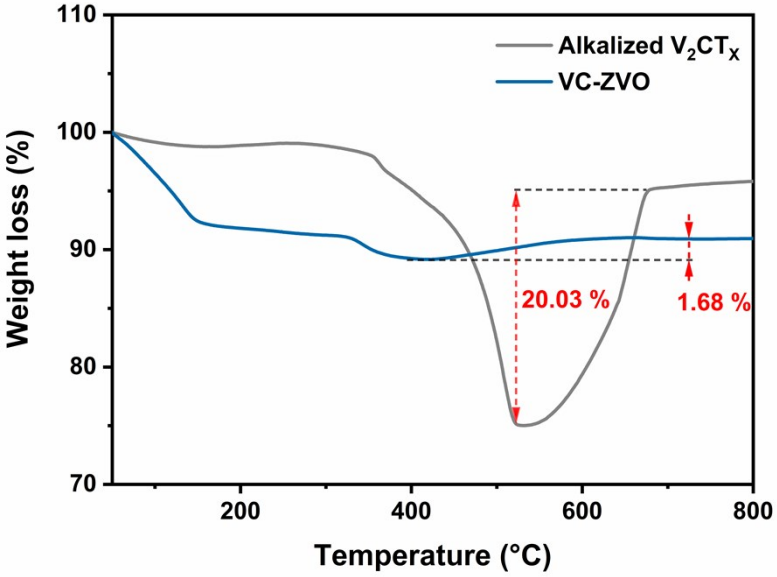

Fig. S4. TGA results for VC−ZVO and alkalized V_2CT_X samples.

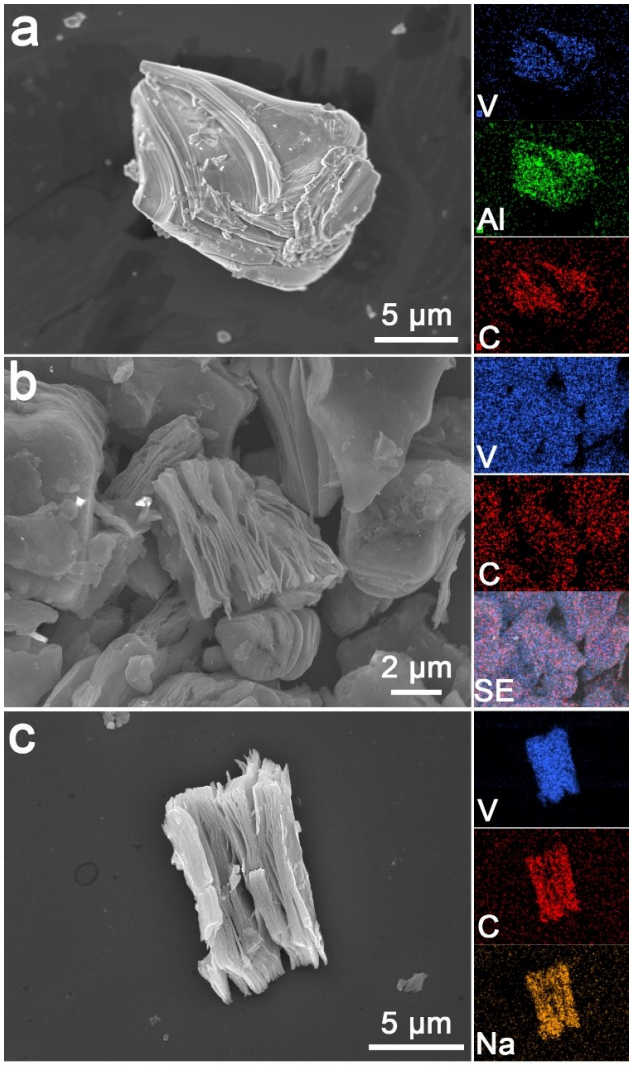

Fig. S5 SEM images and corresponding element mapping of (a) V_2AlC MAX, (b) V_2CT_X MXene, and (c) alkalized V_2CT_X.

The typical SEM image of the V_2AlC MAX dense layered structure is shown in Figure S5a. After etching the Al layer from V_2AlC MAX by HF solution, typical accordion-like V_2CT_X with a smooth surface can be observed (Figure S5b). After alkalization and Na-ion intercalation, the morphology of V_2CT_X still displays a clear multilayer structure (Figure S5c). In addition, corresponding element mapping of alkalized V_2CT_X shows that the V_2CT_X stack is successfully intercalated with Na ions.

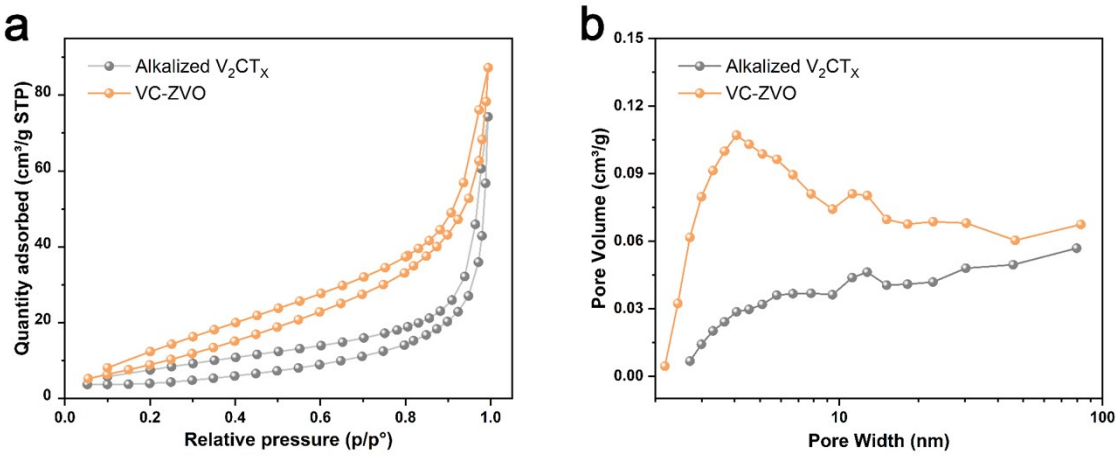

Fig. S6 (a) Nitrogen sorption isotherms. (b) Pore size distribution of alkalized V_2CT_X and VC−ZVO.

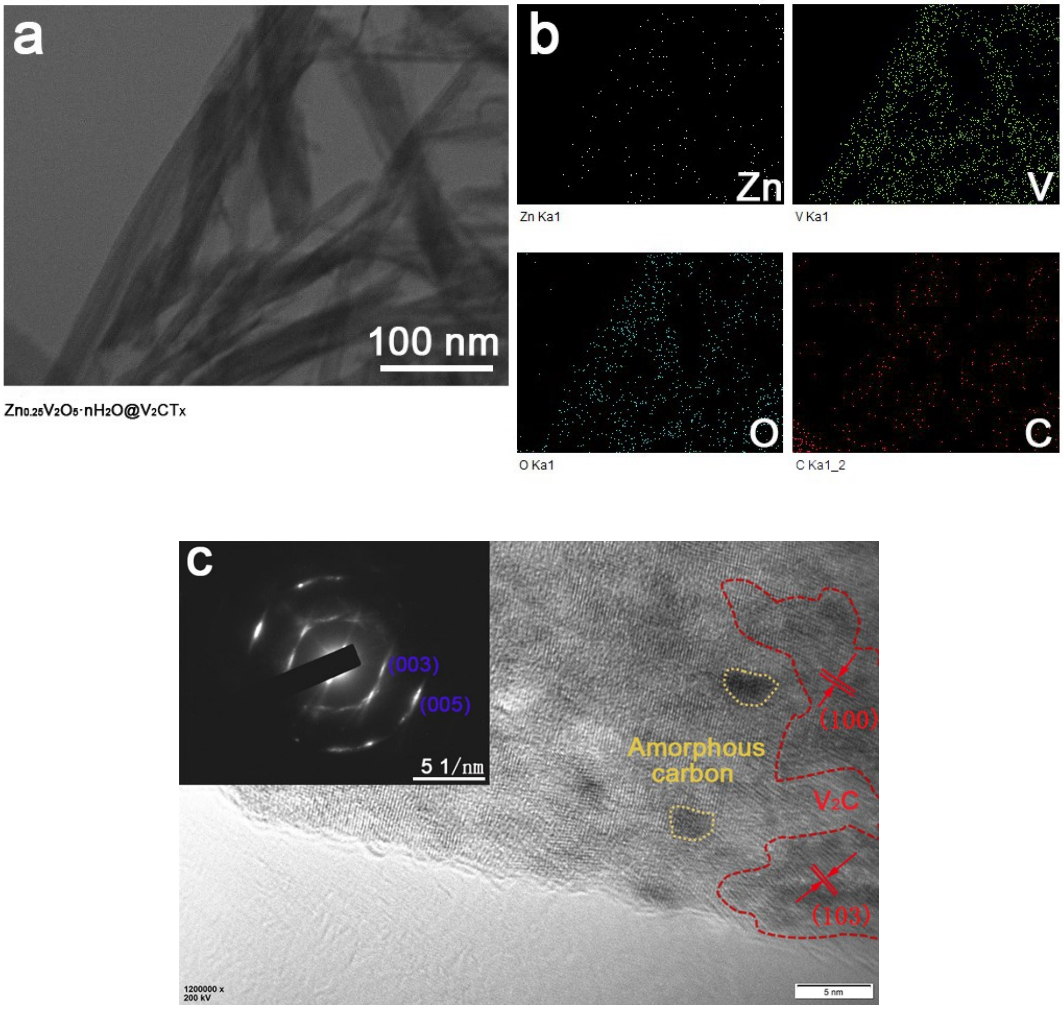

Fig. S7 (a) TEM image of VC−ZVO and (b) corresponding EDX mapping. (c) HRTEM image of VC−ZVO (the inset illustrates the SAED image of ZVO).

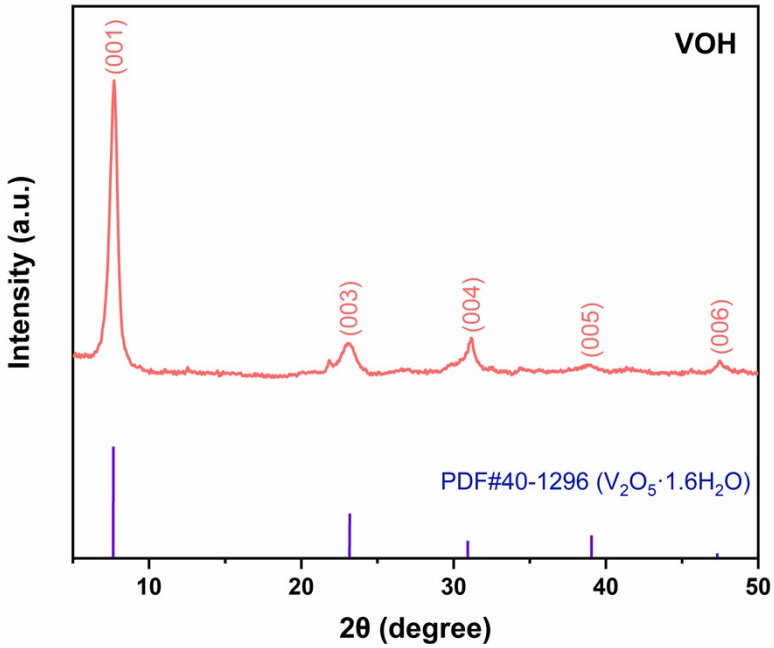

Fig. S8 XRD patterns of VOH.

To study the electrochemical performance and kinetics of VC−ZVO, typical VOH was synthesized by a facile method (more details were shown in the Experimental Section). As shown in Figure S8, the synthetic sample is $V_2O_5 \cdot 1.6H_2O$ (PDF#40-1296),[3] which has a layered structure of hydrated vanadate.

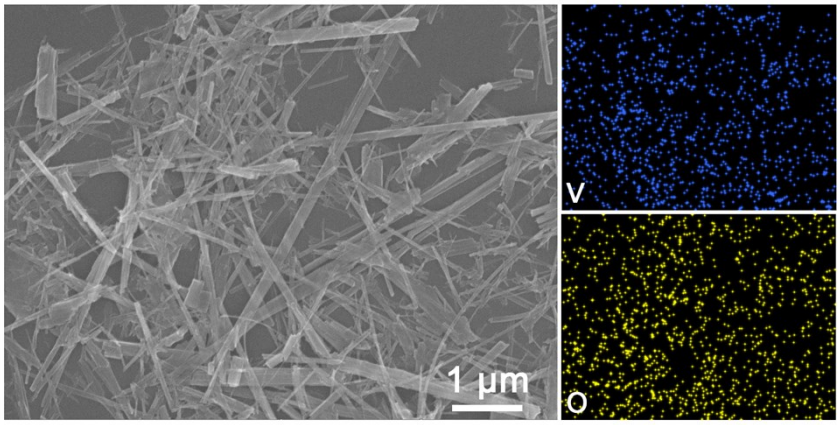

Fig. S9 SEM images of VOH and the corresponding element mapping.

As shown in Figure S9, VOH shows ribbon-like morphology with slight agglomeration and a width around 100 nm, which is consistent with the typical morphology of hydrated vanadate. The corresponding EDX element diagrams show that V and O elements are evenly distributed in the sample.

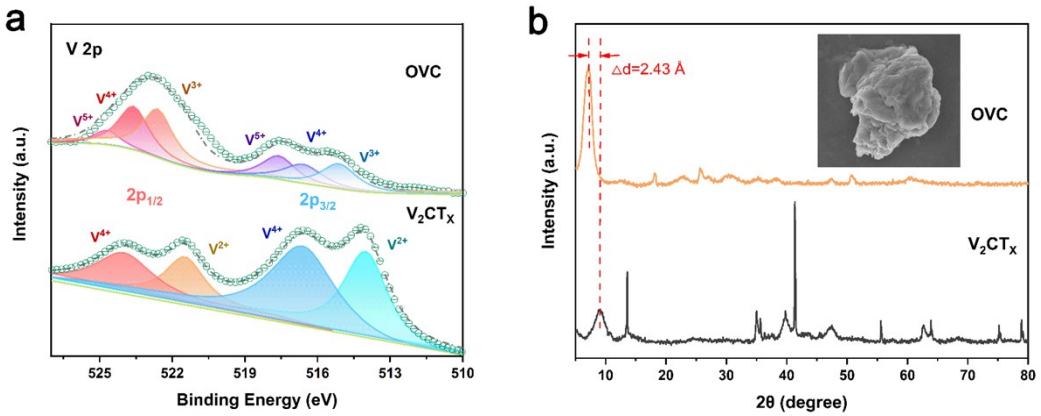

Fig. S10 (a) XPS spectra and (b) XRD pattern of OVC and V_2CT_X (the inset illustrates the SEM image of OVC).

The oxidation treatment leads to the valence-state rise of V_2CT_X MXene, as shown by the detailed XPS spectra of V 2p in Figure S10a. Specifically, V^{5+} of OVC appears and becomes stronger, and the $V^{5+}/V^{4+}/V^{3+}$ ratio matches the desirable phase transition.[4] Figure S10b shows the XRD patterns of OVC and V_2CT_X. Compared with the diffraction peak of V_2CT_X, the (002) peak of OVC becomes sharper and shifts down to 7.25° after oxidation treatment, indicating that water molecules intercalate V_2CT_X further. Moreover, the characteristic diffraction peaks of V_2AlC and V_2CT_X almost disappear, and diffraction peaks of vanadium oxide and carbon appear. As shown in the inset of the SEM image, OVC presents the accordion-like structure of V_2CT_X. Interestingly, due to the growth of the oxidized coating, the sharp edges and smooth surfaces of the original V_2CT_X become blurred and rough after the oxidation treatment. In the absence of pre-intercalated Zn^{2+} as template, the oxidized V_2CT_X could not be transformed into layered hydrated vanadate with the nanobelt morphology.

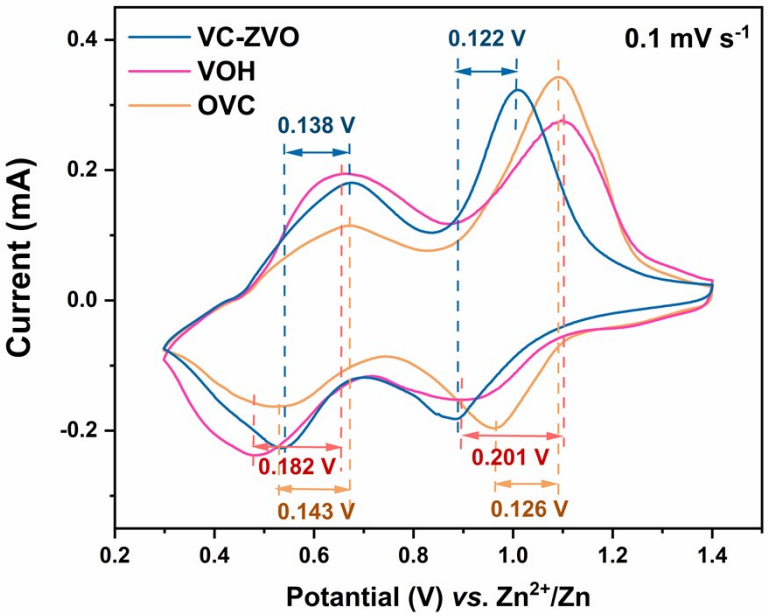

Fig. S11. Comparison of the 2nd CV curves of VC−ZVO, VOH and OVC at 0.1 mV s^{-1}.

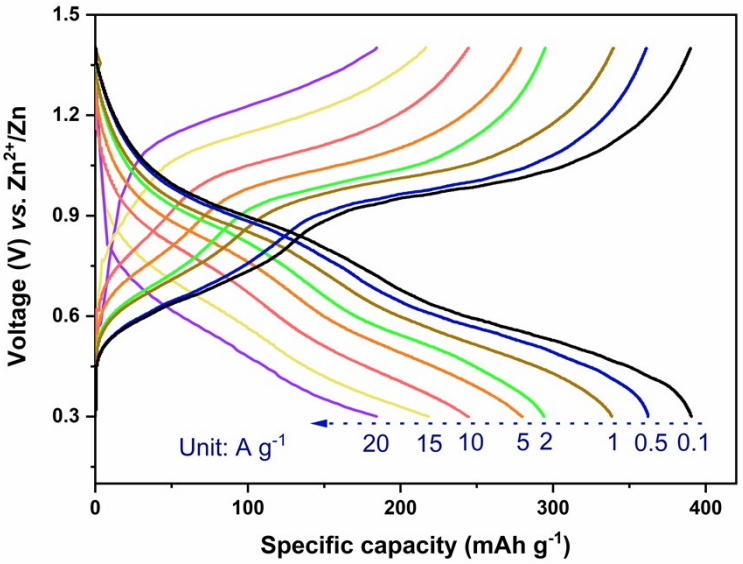

Fig. S12. Galvanostatic charge and discharge curves under various current densities for the VC−ZVO electrodes.

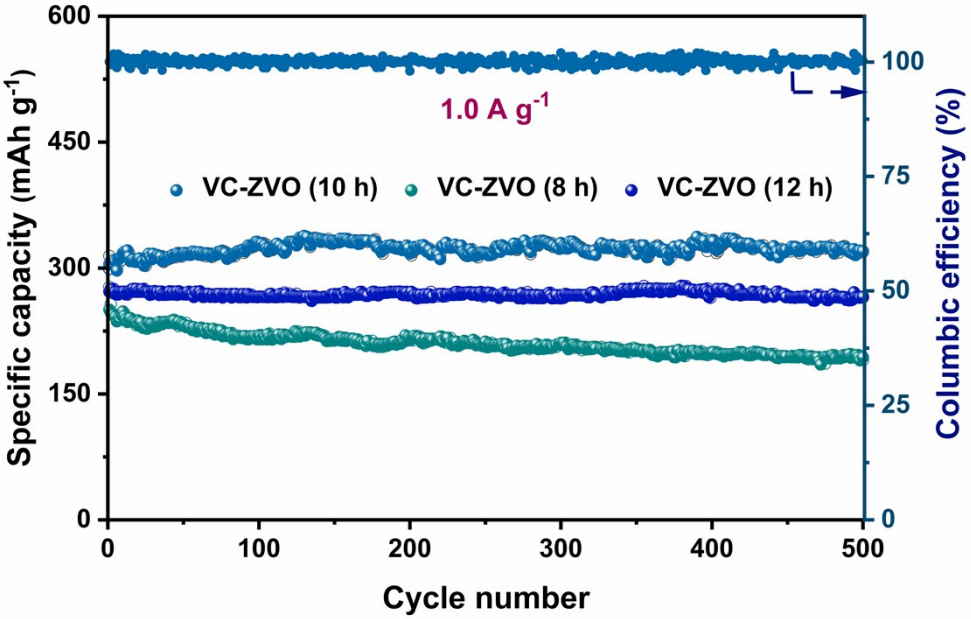

Fig. S13. Cycling performance of VC−ZVO obtained after different reaction time at 1.0 A g^{-1}.

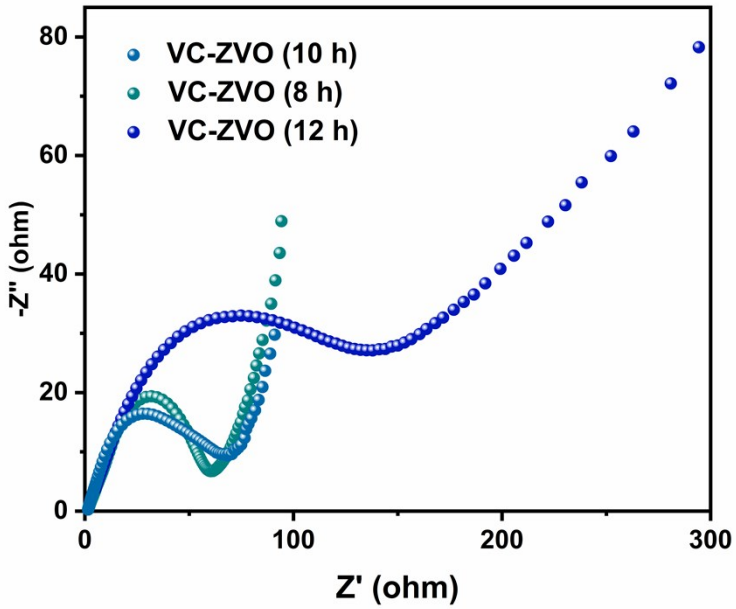

Fig. S14. EIS spectra of VC−ZVO obtained after different reacction time.

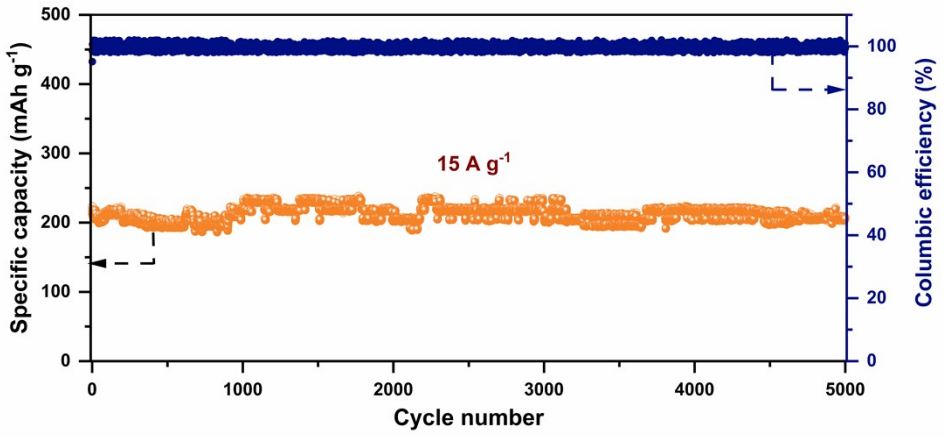

Fig. S15. Cycling performance of high current density of the VC−ZVO electrode at 15 A g^{-1}.

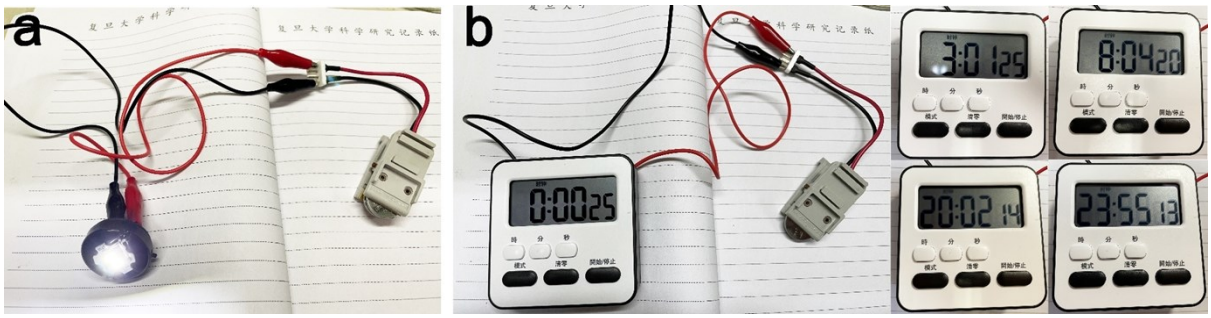

Fig. S16. (a) LED indicator powered by two cells. (b) Electronic timer powered by one cell.

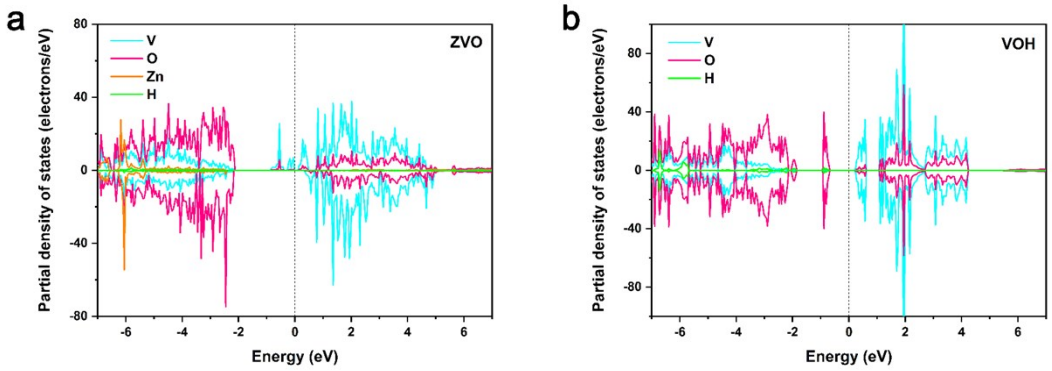

Fig. S17. Density of states for (a) ZVO and (b) VOH.

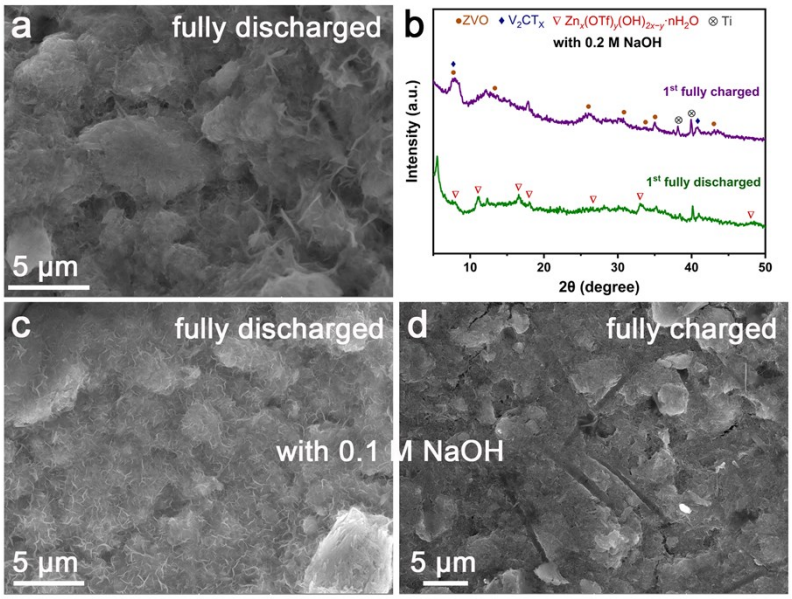

Fig. S18. (a) *Ex situ* SEM image of of the VC−ZVO electrodes at the fully discharged state. (b) *Ex situ* XRD patterns of of the VC−ZVO electrodes with 0.1 M NaOH electrolyte additive at different states. *Ex situ* SEM image of of the VC−ZVO electrodes with 0.1 M NaOH electrolyte additive at (c) the fully discharged state and (d) the fully charged state.

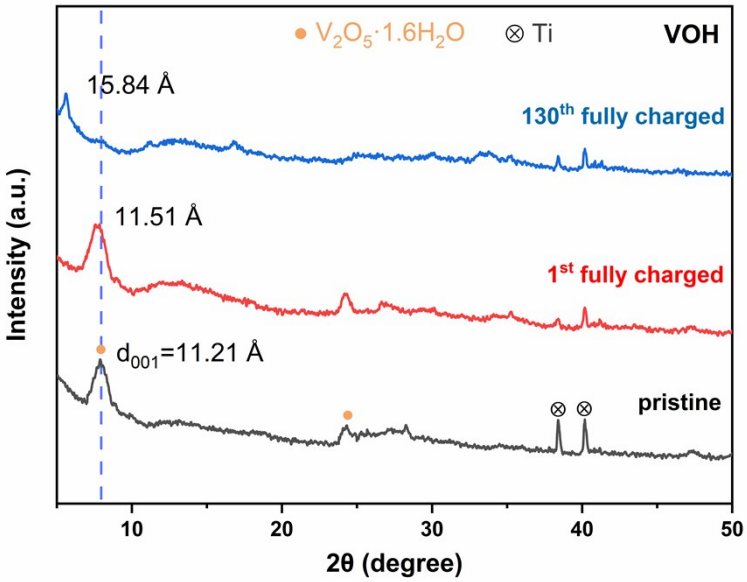

Fig. S19. *Ex situ* XRD patterns of the VOH electrodes after different cycles at 0.1 A g^{-1}.

The crystal structure stability of the VOH electrodes as controlled samples after different cycles have been investigated (**Fig. S19**). After the first cycle, the (001) plane of VOH shows a slight deviation of 0.19°. Nevertheless, after 130 cycles, the (001) plane of VOH shifts greatly to 5.58°, indicating that the interlayer of VOH is irreversibly expanded and the crystal structure of VOH is destroyed. In addition, the intensity of the diffraction peak of VOH is also relatively weakened, suggesting that part of VOH dissolves during cycling.

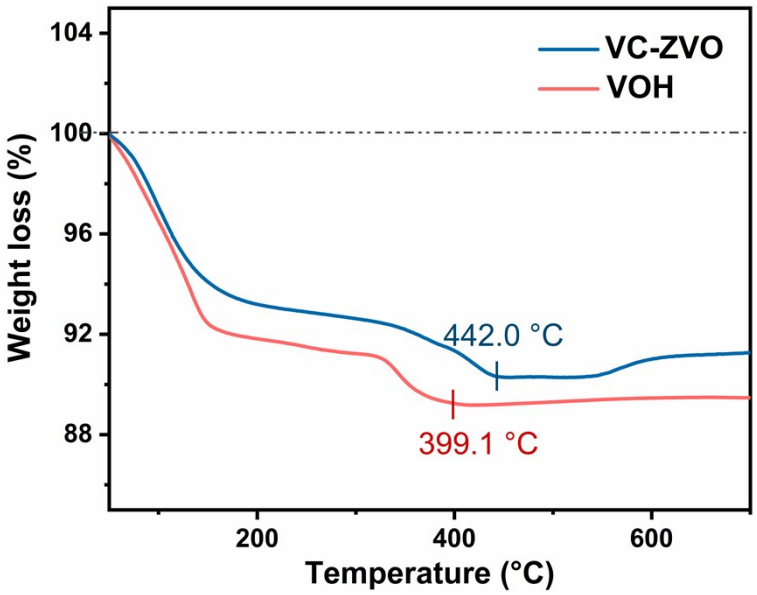

Fig. S20. TGA results for VC−ZVO and VOH samples.

Table S1 Zinc ion diffusion coefficient of representative vanadium-based cathodes.

Cathode	Electrolyte	D (cm^2 s^{-1})	Reference
VC−ZVO	**3 M $Zn(CF_3SO_3)_2$**	**1.3×10^{-7}–6.3×10^{-8}**	**This work**
$Zn_{0.25}V_2O_5$.nH2O	1 M $ZnSO_4$	10^{-9}–10^{-10}	5
$V_5O_{12}\cdot6H_2O$	3 M $Zn(CF_3SO_3)_2$	10^{-10}–10^{-11}	6
$LixV_2O_5\cdot nH_2O$	2 M $ZnSO_4$	3.37×10^{-8}–3.3×10^{-9}	7
$Cu_{0.1}V_2O_5\cdot0.08H_2O$	2 M $ZnSO_4$	10^{-8} –10^{-9}	8
PEDOT-$NH_4V_3O_8$	3 M $Zn(CF_3SO_3)_2$	5.3–6.4×10^{-9}	9

Reference

1 A. Jain, G. Hautier, C. J. Moore, S. P. Ong, C. C. Fischer, T. Mueller, K. A. Persson and G. Ceder, Comput. Mater. Sci. 2011, 50, 2295-2310.

2 C. Wang, H. Xie, S. Chen, B. Ge, D. Liu, C. Wu, W. Xu, W. Chu, G. Babu, P. M. Ajayan and L. Song. Adv. Mater. 2018, 30, 1802525.

3 Z. Cao, X. Zhu, D. Xu, P. Dong, M. O. L. Chee, X. Li, K. Zhu, M. Ye and J. Shen. Energy Storage Mater. 2020, 36, 132-138.

4 X. Li, M. Li, Q. Yang, G. Liang, Z. Huang, L. Ma, D. Wang, F. Mo, B. Dong, Q. Huang and C. Zhi. Adv. Energy Mater. 2020, 2001791.

5 D. Kundu, B. D.Adams, V. Duffort, S. H. Vajargah and L. F. Nazar, Nat. Energy 2016, 1, 16119.

6 N. Zhang, M. Jia, Y. Dong, Y. Wang, J. Xu, Y. Liu, L. Jiao and F. Cheng, Adv. Funct. Mater. 2019, 29, 1807331.

7 Y. Yang, Y. Tang, G. Fang, L. Shan, J. Guo, W. Zhang, C. Wang, L. Wang, J. Zhou and S. Liang, Energy Environ. Sci., 2018, 11, 3157-3162.

8 Y. Yang, Y. Tang, S. Liang, Z. Wu, G. Fang, X. Cao, C. Wang, T. Lin, A. Pan and J. Zhou, Nano Energy 2019, 61, 617.

9 D. Bin, W. Huo, Y. Yuan, J. Huang, Y. Liu, Y. Zhang, F. Dong, Y. Wang and Y. Xia, Chem 2020, 6, 968.